

## Article

# Combined Acoustic Emission and Digital Image Correlation for Early Detection and Measurement of Fatigue Cracks in Rails and Train Parts under Dynamic Loading

Alexander Machikhin <sup>1,2</sup>, Anton Poroykov <sup>1</sup>, Vladimir Bardakov <sup>1,3</sup>, Artem Marchenkov <sup>1,\*</sup>, Daria Zhgut <sup>1</sup>, Milana Sharikova <sup>1,2</sup>, Vera Barat <sup>1,3</sup>, Natalia Meleshko <sup>1</sup> and Alexander Kren <sup>4</sup>

<sup>1</sup> Moscow Power Engineering Institute, 14, Krasnokazarmennaya Str., 111250 Moscow, Russia

<sup>2</sup> Scientific and Technological Center of Unique Instrumentation, Russian Academy of Sciences, 15, Butlerova Str., 117342 Moscow, Russia

<sup>3</sup> INTERUNIS-IT, POB 140, 20B, Shosse Entusiastov, 111024 Moscow, Russia

<sup>4</sup> Institute of Applied Physics, National Academy of Sciences, 16, St. Akademicheskaya, 220072 Minsk, Belarus

\* Correspondence: art-marchenkov@yandex.ru; Tel.: +7-967-123-7576

**Abstract:** Fatigue crack in rails and cyclic-loaded train parts is a contributory factor in multiple railroad accidents. We address the problem of crack detection and measurement at early stages, when total failure has not yet occurred. We propose to combine acoustic emission (AE) testing for prediction of crack growth with digital image correlation (DIC) for its accurate quantitative characterization. In this study, we imitated fatigue crack appearance and growth in samples of railway rail and two train parts by cyclic loading, and applied these two techniques for inspection. Experimental results clearly indicate the efficiency of AE in the early detection of fatigue cracks, and excellent DIC capabilities in terms of geometrical measurements. Combination of these techniques reveals a promising basis for real-time and non-destructive monitoring of rails and train parts.

**Keywords:** acoustic emission; digital image correlation; fatigue cracks; crack detection; dynamic loading; non-destructive testing



**Citation:** Machikhin, A.; Poroykov, A.; Bardakov, V.; Marchenkov, A.; Zhgut, D.; Sharikova, M.; Barat, V.; Meleshko, N.; Kren, A. Combined Acoustic Emission and Digital Image Correlation for Early Detection and Measurement of Fatigue Cracks in Rails and Train Parts under Dynamic Loading. *Sensors* **2022**, *22*, 9256. <https://doi.org/10.3390/s22239256>

Academic Editors: Yanfeng Shen, Cuixiang Pei and Hongchen Miao

Received: 26 October 2022

Accepted: 26 November 2022

Published: 28 November 2022

**Publisher's Note:** MDPI stays neutral with regard to jurisdictional claims in published maps and institutional affiliations.



**Copyright:** © 2022 by the authors. Licensee MDPI, Basel, Switzerland. This article is an open access article distributed under the terms and conditions of the Creative Commons Attribution (CC BY) license (<https://creativecommons.org/licenses/by/4.0/>).

## 1. Introduction

Fatigue fractures of rails, wheelsets, solid-rolled wheels, side frames of wagon bogies, and other parts of the rolling stock frequently trigger railway accidents and incidents [1–3]. Despite the wide range of non-destructive testing (NDT) techniques applied in regular inspection of these parts, early detection and quantitative characterization of fatigue cracks is still an important task. Complex geometric shapes, thermal loading, subjectivity of decision-making, and other factors significantly complicate the analysis and prediction of fatigue crack growth in the parts of the rolling stock [4–6]. Conventional NDT methods include ultrasonic, eddy current, magnetic, and X-ray, utilize the signals reflected from the local inhomogeneities, and, thus, have relatively low sensitivity in terms of complex-shaped crack-like defects [7–9].

Unlike these methods, acoustic emission (AE) testing is a technique based on the analysis of elastic waves generated by the defects initiation and growth. In comparison with conventional NDT methods, AE testing has a number of advantages. It is insensitive to the shape and orientation of the defects, does not require spatial scanning, and thus is well suited for in situ structural health monitoring [10,11]. AE sources include plastic deformation, initiation and growth of cracks, fracture, corrosion, leakages, fiber debonding, etc. [10]. AE technique is widely used and well-proven in detecting the processes of fatigue cracks initiation and growth both in metallic and composite materials [12–16].

AE testing has been successfully applied to fatigue crack detection in rails under operational loads [17,18]. The development of advanced AE data processing algorithms

significantly expands the scope of its applications for testing and detection of fatigue cracks in rails. Furthermore, in [19,20] authors used wavelet analysis to extract the signals from even small fatigue cracks hidden below the background noise. Deep learning and neural network processing enabled detection and localization of the defects in the head, web, and foot of the rail [21]. Regarding the parts of the rolling stock, AE testing exhibits high efficiency in detection and monitoring fatigue cracks in full-scale railway axles [22–24]. AE technique, combined with an automated loading system, has also been successfully applied to fatigue crack detection in molded pieces of rolling stock, such as the side frame and bolster of railway bogies [25,26].

In addition to identification of the defects and their growth prediction, it is important to measure their size and location. For this purpose, AE testing has to be coupled with a well-established method for geometrical measurements. One of the most promising techniques for quantifying defects in combination with AE testing is digital image correlation (DIC).

DIC is a non-contact full-field optical technique for deformation diagnostics and quantitative assessment of surface defects with high spatial resolution and accuracy [27]. It is widely in use to verify various NDT methods: ultrasound, eddy current, etc. [28–30]. DIC is also an effective complement to AE testing of concrete [31], reinforced concrete [32,33], metals [34,35], welded joints [36], etc. DIC may be used to confirm the cracking point determined by the AE testing [34,35], as well as identification of different damage mechanisms (plastic deformation, crack initiation, and propagation) based on comparison AE and DIC data [36–39]. DIC is also suitable for full-scale testing, including railway equipment [40], but this application is still limited due to limited field of view, specific calibration, etc.

In this study, we propose to implement DIC after primary information on the presence and location of defects is collected by AE testing, either in lab or out-of-lab environment. Further characterization and quantification of defects must be carried out by DIC under conditions close to operation. The proposed approach is thus a compromise between possible qualitative determination of defects in the field conditions and high-precision defect measurement under laboratory conditions.

A combined AE–DIC approach might be especially effective for monitoring the rolling stock parts due to their large dimensions, shape complexity, and operation under cyclic loading. In this study, we attempt to validate it by detection and quantitative characterization of fatigue cracks in samples of rails, wheelsets, and traction clamps.

## 2. Experimental Protocol

Acronyms and symbols introduced in the manuscript and their definitions are presented in Table 1.

**Table 1.** List of acronyms and symbols used in the study.

Acronym	Description	Symbol	Description
NDT	non-destructive testing	$\sigma_y$	yield strength
AE	acoustic emission	$\sigma$	cycle amplitude
DIC	digital image correlation	$l$	position of the AE source
EDM	electrical discharge machining	$dl_{AE}$	inaccuracy of the AE source position
$\varepsilon$	maximum normal strain	$N$	number of AE events
$V_x$ and $V_y$	displacements detected by DIC	$\eta_{TAE}$	ratio of $N_{max}$ and $N_{mean}$ , when the crack is detected

Table 1. Cont.

Acronym	Description	Symbol	Description
$\epsilon_{TDIC}$	threshold value defined by transition from elastic deformation to plastic in the notch area	$N_{max}$	location maximum of histogram
$s_{DIC}$	crack's dimension as a length of skeletonized line obtained after processing the field of maximum normal strain	$N_{mean}$	mean value over all intervals, except for the maximum
$f$	focal length of the lens	$T_{AE}$	moment of crack appearance
$L$	distance to the inspected sample	$T_{DIC}$	moment of crack initiation
$\Delta$	pixel pitch of the camera	$\epsilon_x$	deformation in $x$ directions
$n$	measured crack's length in pixels	$\epsilon_y$	deformation in $y$ directions

### 2.1. Samples Preparation

For our experiments, we prepared samples from three railway parts: rail, wheelset, and traction clamp. The rail was made of E76F high-carbon steel and experiences mainly compressive stresses from the train. The wheelset, together with two steel wheels, forms part of the wagon cart. The wheelset material experiences cyclic bending stresses. The wheelset was made of OsV carbon steel. A traction clamp is necessary to connect wagons to each other. During operation, this element experiences mainly cyclic tensile and bending loads when the train starts moving. The traction clamp was made of low-alloy structural steel 20GL. The chemical composition of these materials presented in Table 2.

Table 2. Chemical composition of the test samples' materials.

Part	Steel	Composition, wt. %					
		C	Si	Mn	V	S	P
Rail	E76F	0.71–0.82	0.25–0.60	0.75–1.15	0.03–0.15	$\leq 0.025$	$\leq 0.025$
Wheelset	OsV	0.40–0.48	0.15–0.35	0.55–0.85	-	$\leq 0.045$	$\leq 0.04$
Traction clamp	20GL	0.15–0.25	0.20–0.40	1.20–1.60	-	$\leq 0.04$	$\leq 0.04$

Samples from the rail (3 pcs) were sections 10 mm thick (Figure 1a). U-notches of 0.25 mm width and 2 mm depth were produced in its web part by wire electrical discharge machining (EDM), since this does not require additional hardening of the metal surface. To make a notch of the required depth with a radius at the top of 0.25–0.3 mm, we applied a wire of 0.25 mm diameter. Samples cut from the wheelset (3 pcs) were 20 × 25 × 350 mm bars with notches of 3–5 mm depth and 0.25–0.3 mm radius, produced by EDM (Figure 1b). Samples made from the traction clamp (3 pcs) were 3 mm thick plates with lateral notches, obtained with EDM by wire cutting along a defined contour (Figure 1c). As polished metal does not have the high-contrast surface texture necessary for digital image correlation (DIC) method application, we created a random pattern on one of the samples' surfaces using white and black spray paint.

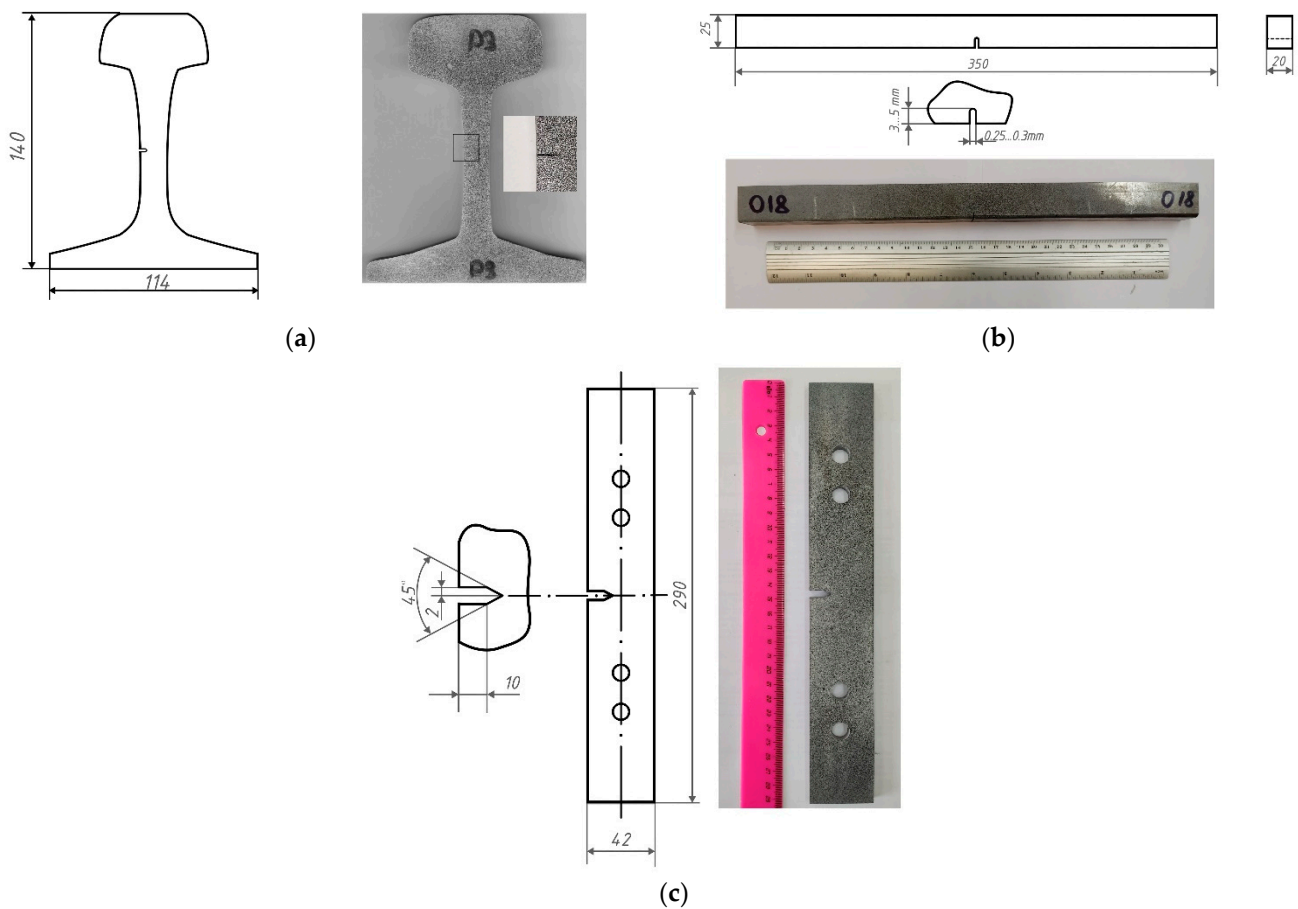


**Figure 1.** Schemes and photos of the samples made from rail (a), wheelset (b), and traction clamp (c).

## 2.2. Experimental Setup

The experimental setup was based on the servo-hydraulic fatigue testing system Instron 8801, which was necessary to imitate cyclic loading caused by the train movement. The loading scheme was designed in order to imitate the loads that studied parts experience during operation, i.e., the rails were subjected to compressive load, the samples from the wheelset to three-point bending, and the samples from the traction clamp to tensile loading. We fixed the rail samples using grips (Figure 2a). Wheelset samples were placed on a three-point static bending fixture (Figure 2b), including two lower supports separated by 250 mm distance, and an upper cylindrical punch with a diameter of 10 mm. Samples from the traction clamp were installed with grips through damping pads (Figure 2c).

Figure 3 shows fatigue stress cycles applied to the samples. Sinusoidal loading was necessary to ensure the smooth running of the punch in the testing machine when reaching the minimum and maximum values of the cycle. This reduced the level of acoustic noise that occurred in the testing machine when passing through the extreme points of the cycle, thus minimizing the amplitude threshold for the recorded AE signals. Maximal stress was limited by the yield strength of the material  $\sigma_y$  at the level  $(0.48 \dots 0.72)\sigma_y$ . This is close to the values of maximum allowable stresses that may occur during operation of the inspected elements. Under such stress, in the absence of notches and cracks, the structural elements stay in the elastic region during operation. In the presence of cracks, or severe stress concentrators, plastic deformation and subsequent destruction occur with high probability. The loading frequency 5 Hz was a good compromise between the duration of the experiment, the acoustic noise level, which increases in the testing machine with the raise of the loading frequency, and the duration of the tests. Loading conditions applied to the samples are specified in Table 3. Loading was accompanied with continuous recording of DIC and AE data.

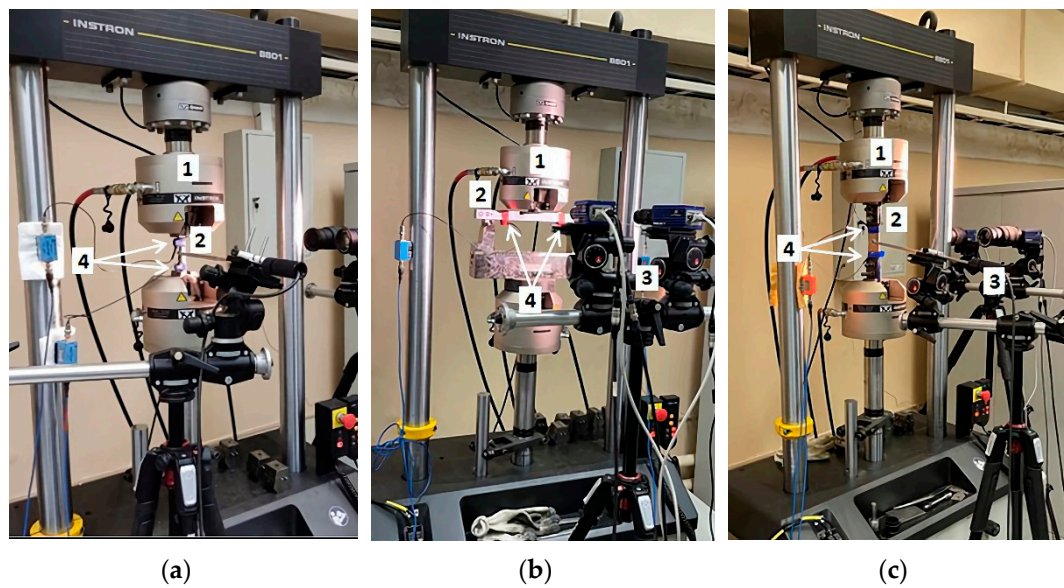


**Figure 2.** Experimental setup with rail (a), wheelset (b), and traction clamp (c) samples under inspection: 1, loading device (punch); 2, inspected sample; 3, DIC system; 4, AE sensors.

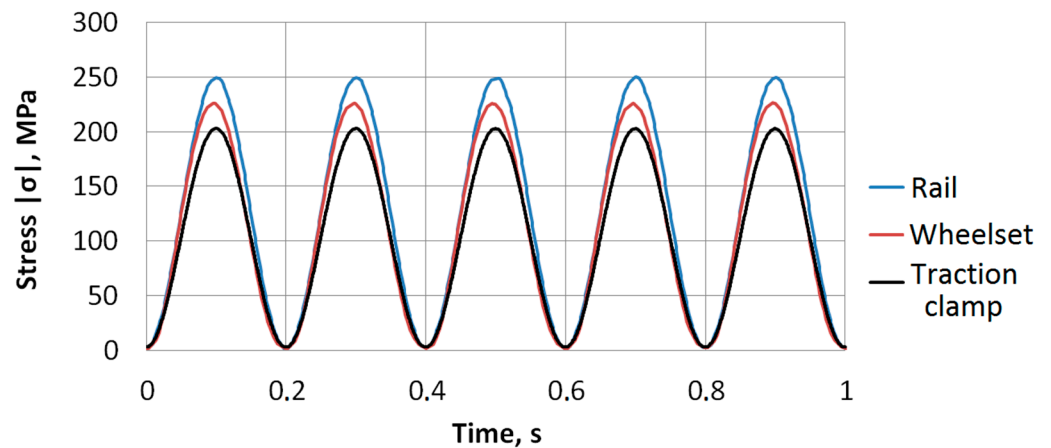


**Figure 3.** Loading cycles applied to the inspected samples.

**Table 3.** Loading conditions applied to the samples.

Part	Type of Stress	Cycle	Frequency, Hz	Cycle Amplitude $\sigma$ , MPa	Material Yield Stress $\sigma_{y1}$ , MPa	$\sigma/\sigma_y$
Rail	Compressive	Sinusoidal	5	250	520	0.48
Wheelset	3-point bending			230	320	0.72
Traction clamp	Tensile			200	360	0.55

We installed two AE sensors GT200 (GlobalTest) with a resonant frequency of 180 kHz on each sample, symmetrically, with respect to the stress concentrator, and connected them to the preamplifier with 26 dB gain. To achieve acoustic contact between the AE sensors and the sample, we used Lithol-24 as an intermediate layer. The AE system A-Line 32D PCI (INTERUNIS-IT) acquired the acoustic signals with a frequency range of 100–400 kHz.

For DIC measurements, we used the machine vision system StrainMaster (LaVision). It consists of PC with DaVis 8.4 software (LaVision GmbH, Göttingen, Germany), a synchronization unit, and two monochrome cameras Imager SX (2/3", 2456 × 2058, 12 bit) equipped

with lenses Sigma ( $f = 18\text{--}200$  mm, 1:3.5–6.3). Each experiment included  $2400 \times 1300$  image acquisition of a  $50 \times 40$  mm sample's notched area at 20 fps, their joint processing by DIC algorithms, and calculating the strain maps  $\varepsilon(x,y)$ .

### 2.3. Data Processing

To determine the AE signals caused by fatigue crack's initiation and growth, we used linear location of AE sources and placed AE sensors at the edges of the samples to be able to locate AE sources within the maximal area. The distance between them was 50 mm for the rail, 160 mm for the wheelset, and 60 mm for the clamp. The linear location algorithm provided the position  $l$  of the AE source located on the line between AE sensors. Dependence of the number of AE events  $N$  on  $l$  vividly illustrates such an approach. Due to typical sound velocity, 3000 m/s, in the inspected steels and sampling step  $1 \mu\text{s}$ , the inaccuracy  $dl_{\text{AE}}$  of measured  $l$  was about 3 mm. Therefore, the distance between AE sensors for linear location algorithm was divided into 3 mm intervals. This was rather coarse for accurate measurements, but was enough for navigating a fine tool with higher accuracy to the area of the crack for detailed metrological inspection. To identify the moment  $T_{\text{AE}}$  of crack appearance, the threshold criterion [41] was applied. For each new AE event, we evaluated its position and updated the location histogram. Then, the ratio of the location maximum  $N_{\text{max}}$  of histogram to the mean value  $N_{\text{mean}}$  over all intervals, except for the maximum, was calculated. A crack was considered to be detected when the maximum  $N_{\text{max}}$  in the histogram was  $\eta_{T_{\text{AE}}}$  times greater than the mean value  $N_{\text{mean}}$ , i.e.,

$$N_{\text{max}}/N_{\text{mean}} \geq \eta_{T_{\text{AE}}}, \quad (1)$$

The upper row of Figure 4 shows the histograms  $N(l)$  for all three types of the inspected samples at the moment  $T_{\text{AE}}$  when  $\eta_{T_{\text{AE}}} = 3$ . At this empirical threshold, it was possible to distinguish a clear maximum. Its location corresponds to the crack position in the experiments. We can see that this threshold corresponds well to the signal level well above the emissivity of the inspected materials.

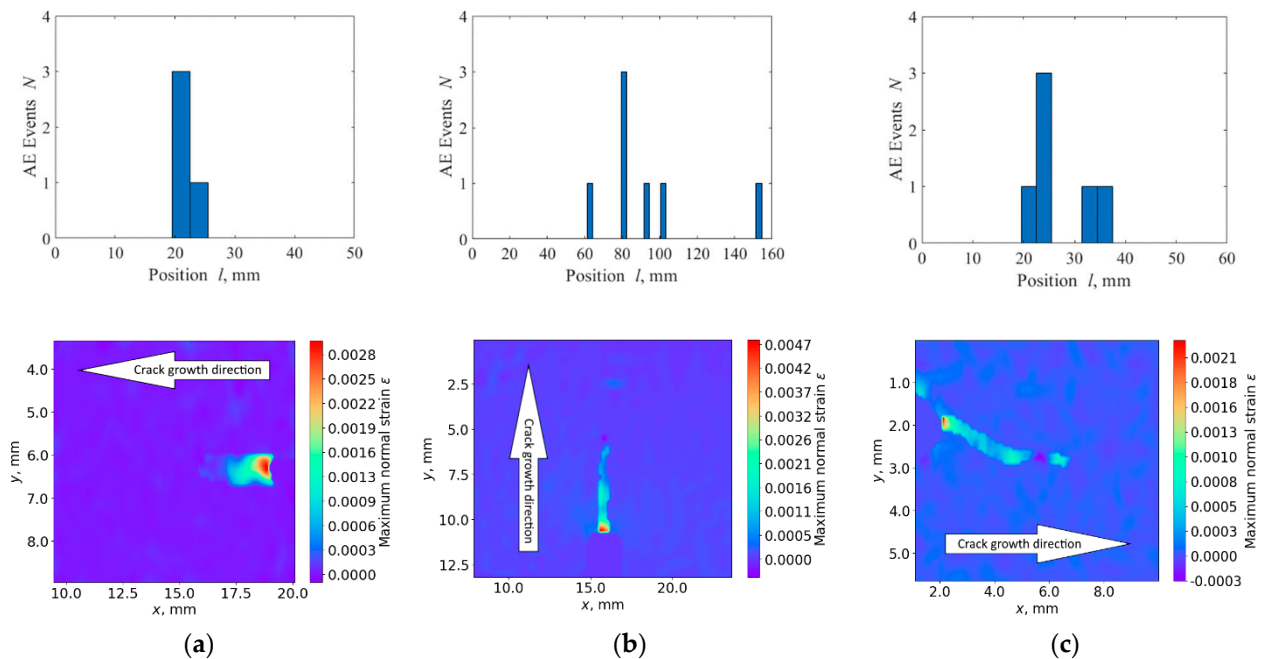


**Figure 4.** AE ( $N(l)$ , upper row) and DIC ( $\varepsilon(x,y)$ , lower row) data for rail (a), wheelset (b), and traction clamp (c) samples at the moments  $T_{\text{AE}}$  and  $T_{\text{DIC}}$ , respectively.

The DIC method was necessary to obtain information about the deformation of the samples during their mechanical tests. It was based on the comparison of the images of

the sample surface. The first (reference) image was taken before the test. In this image, the surface is considered to be deformation-free. The second image was captured during the test, when the sample was loaded. Quantifying its difference, with respect to the reference, provided an estimate of the deformation that the sample experienced under loading.

In this study, we used the least squares matching algorithm, together with the region grow algorithm. First, initial (seeding) points on the surface of the sample were set. For them, an affine transformation of a small area (interrogation window) around the point in the original image was searched. After matching was achieved, similar search was performed for neighboring areas, remote from the original one by a given step. The starting approximation obtained for the initial point was necessary to find their affine transformation. Thus, the calculation area increased iteratively with respect to each initial point. The affine transformation allows estimating the sample surface deformation in pixel units and recalculating them into real dimensions (mm/ $\mu\text{m}$ ) using the camera calibration data.

User-defined inputs for image processing with DIC were the size of the interrogation window, the step for splitting into windows, and the coordinates of the initial points. There were also additional settings for adjusting the speed-to-precision ratio, mainly affecting the intermediate filtering of the affine transforms. The main parameter for processing was the size of the interrogation window. Its assignment determines the ratio of spatial resolution and measurement error. Smaller windows lead to a higher spatial resolution, but also to a higher uncertainty. Processing used a window size of 29 to 35 pixels depending on the sample, with a step size of 4 to 8 pixels. Typical error for a window size of 31 pixels is 0.005 pixels.

To determine appearance of the crack and evaluate its dimensions from DIC data, we implemented the technique based on maximum normal strain measurement from displacement vector fields [42]:

$$\varepsilon = \frac{\varepsilon_x + \varepsilon_y}{2} + \sqrt{\left(\frac{\varepsilon_x - \varepsilon_y}{2}\right)^2 + \gamma_{xy}^2} \quad (2)$$

where  $\varepsilon_x = dV_x/dx$  and  $\varepsilon_y = dV_y/dy$  are deformations in  $x$  and  $y$  directions,  $V_x$  and  $V_y$  are displacements detected by DIC, and  $\gamma_{xy} = (dV_x/dy + dV_y/dx)/2$  is shear strain.

Processing the scalar normal strain fields includes binarization using Otsu thresholding algorithm and skeletonization. This enables accurate segmentation of the crack area. To determine the moment of crack initiation  $T_{\text{DIC}}$ , we calculated the maximum normal strain  $\varepsilon$  in this area and compared it with the threshold  $\varepsilon_{\text{TDIC}}$  defined by the transition from elastic deformation to plastic in the notch area [43]. If we neglect the small value of material's plastic deformation at this level, then the threshold value  $\varepsilon_{\text{TDIC}}$  is close to the ratio  $\sigma_y/E$ . From tensile tests of the studied materials, the values of the yield stress are  $\sigma_y \approx 520$  MPa for the rail,  $\sigma_y \approx 320$  MPa for the wheelset, and  $\sigma_y \approx 360$  MPa for the clamp. The elastic modulus for all materials is  $E \approx 210,000$  MPa. Thus, the resulting threshold values are  $\varepsilon_{\text{TDIC}} = 0.0025$  for the rail,  $\varepsilon_{\text{TDIC}} = 0.0015$  for the wheelset, and  $\varepsilon_{\text{TDIC}} = 0.0017$  for the traction clamp. As soon as we have

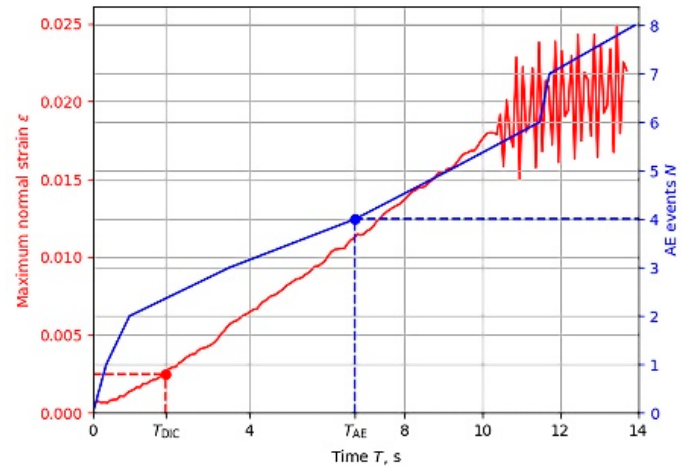
$$\varepsilon > \varepsilon_{\text{TDIC}}, \quad (3)$$

we assume the crack to be detected. The lower row of Figure 4 shows typical strain maps  $\varepsilon(x,y)$  calculated at the moment  $T_{\text{DIC}}$  for all three inspected samples. In these distributions, maximum normal strain  $\varepsilon$  is equal to the threshold value  $\varepsilon_{\text{TDIC}}$ . We may see that this criteria is quite reliable in terms of crack detection, but the DIC system needs accurate positioning, and, thus, has to be navigated to the area of the crack by preliminary AE measurements. This is the basis of the proposed two-stage approach to the detection and quantitative evaluation of fatigue cracks.

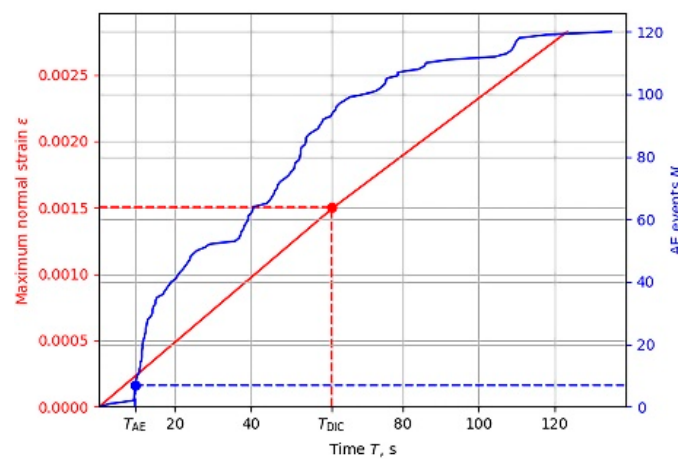
### 3. Results

To validate this approach, we applied the described experimental and data processing techniques to all nine samples. Each experiment included continuous acquisition of AE and

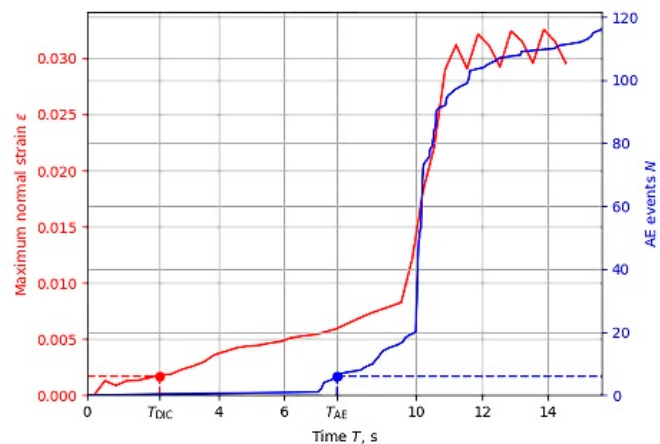
DIC data, evaluation of AE events number  $N$  and maximum normal strain  $\varepsilon$ , verification of criteria (1) and (3) fulfillment, and measurements of crack location and dimension. Figure 5 shows the typical temporal dependences of  $N$  and  $\varepsilon$  for all three types of inspected samples. Time interval of data acquisition covers the moments  $T_{AE}$  and  $T_{DIC}$  of fatigue crack appearance according to (1) and (3), as well as its further growth.



(a)



(b)



(c)

**Figure 5.** Temporal dependencies of AE (blue) and DIC (red) data in rail (a), wheelset (b), and traction clamp (c) samples.

Temporal dependencies of AE events have different shapes that depend on the samples and materials, and correspond to the accumulation of damage processes in the samples. At the moment  $T < T_{AE}$  preceding crack detection by AE testing, not all samples demonstrate a sharp increase in AE events, which corresponds to the appearance of AE source by the destruction process [34]. For a detailed analysis, more AE parameters (energy, counts, and RMS) of recorded events were considered (Figure 6).

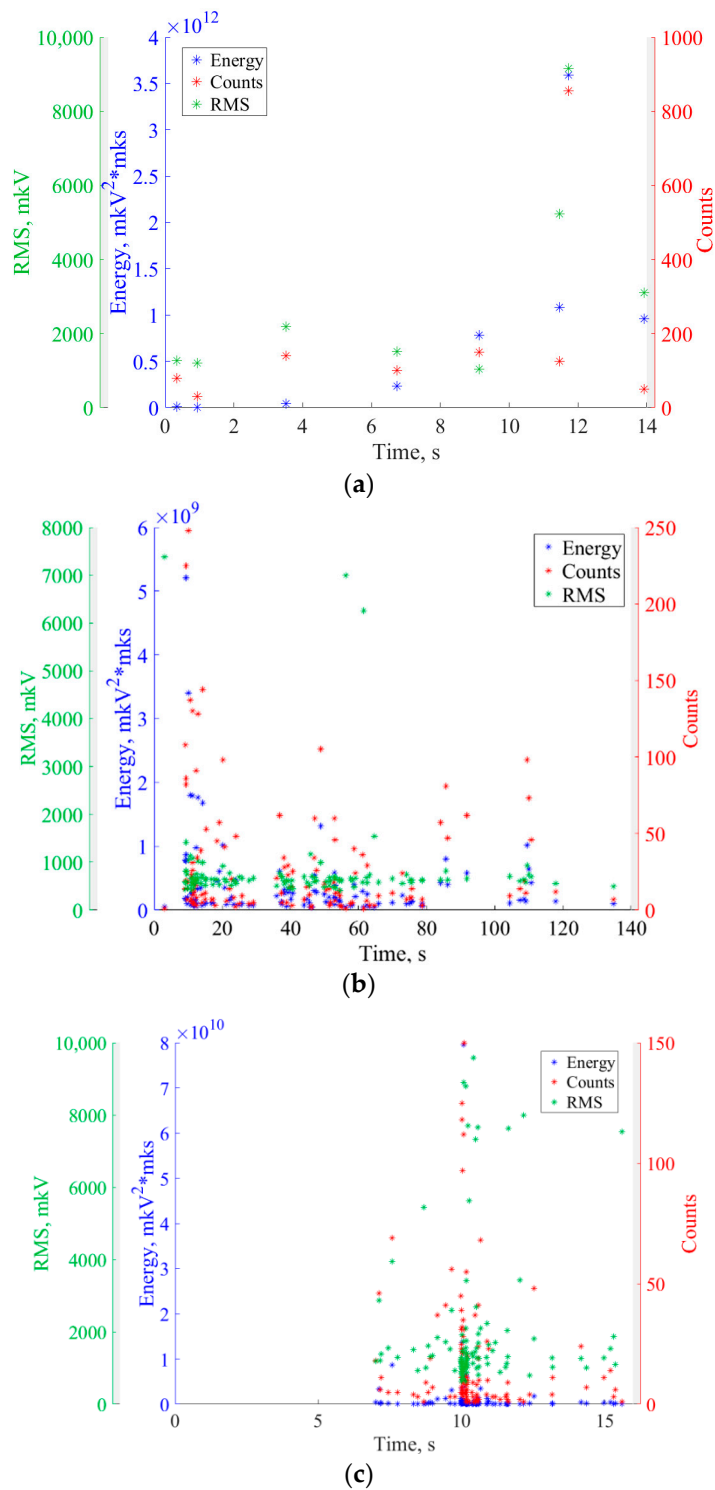


**Figure 6.** Temporal dependencies of AE parameters in rail (a), wheelset (b), and traction clamp (c) samples.

It is well known that a sharp increase in these parameters indicates a crack initiation [44–47]. In all cases, we see such increases. In the wheelset sample, a sharp increase in AE parameters (Figure 6b) coincides with  $T_{AE}$  moment (Figure 5b). In the rail and traction clamp samples, the main peak of AE parameters is observed to have a slight delay with respect to the moment  $T_{AE}$ . This may be explained by a high sensitivity of AE testing to the registration of the early crack initiation processes. Moreover, the fact that the location determined by AE data fits well to the notch position in the samples confirms the correctness of the proposed criterion.

In contrast to  $N(T)$ , temporal dependence of strain  $\varepsilon(T)$  increases monotonically. Its shape does not show definitely the moment  $T_{DIC}$  of crack appearance. This moment is, to a large extent, defined by the threshold  $\varepsilon_{T_{DIC}}$ . That is why we may see that the moment  $T_{AE}$  does not always precede  $T_{DIC}$ , as we might expect (Figure 5b), but  $T_{DIC}$  may be smaller than  $T_{AE}$  (Figure 5a,c). Thus, unlike the AE technique, DIC does not enable objective and evident indication of the moment of fatigue crack appearance, but may provide an objective measure of the crack's geometrical parameters.

We should note that the moments of crack appearance vary depending on the material. In the rail, for example, a crack appears quite early, though the loading is applied in the compression mode with a relatively small cycle load  $0.48 \cdot \sigma_y$ . According to AE data in Figure 5a, a crack appears at  $T_{AE} \approx 7$  s. For comparison, in the wheelset material (Figure 5b), loaded more at  $0.7 \cdot \sigma_y$  level, 3-point bending causes the appearance of tensile stress at the notch tip, and the crack formation time from AE data is somewhat longer ( $T_{AE} \approx 10$  s). This may be caused by differences in the mechanical properties of these materials. Despite higher strength characteristics, the rail material has low ductility, which makes the rail material less resistant to crack initiation and development.

To illustrate the metrological capabilities of DIC, we measured the crack's dimension  $s_{DIC}$  as a length of skeletonized line obtained after processing the field of maximum normal strain  $\varepsilon(x,y)$  (see upper row of Figure 7) and plotted its temporal  $s_{DIC}(T)$  dependence from the moment  $T_{AE}$  (see lower row of Figure 7). Inaccuracy  $ds_{DIC}$  of this measurement, as well as the inaccuracy of crack's position estimation by DIC, may be estimated as

$$ds_{DIC} = dl_{DIC} = (L \cdot \Delta / f) dn, \quad (4)$$

where  $\beta = f/L$  is the linear magnification of DIC optical system,  $L$  is the distance to the inspected sample,  $f$  is the focal length of the lens,  $\Delta$  is the pixel pitch of the camera, and  $n$  is the measured crack's length in pixels.

If we measure the length with inaccuracy  $dn = 1$  pixel, then equation (4) may be simplified:  $ds_{DIC} = dl_{DIC} = \Delta / \beta$ . With respect to our experiments ( $\beta = 0.17$ ,  $f = 170$  mm,  $L = 1$  m,  $\Delta = 3.45 \mu\text{m}$ ), this value is about 0.02 mm, i.e., much smaller than the  $dl_{AE} = 3$  mm measured by AE.

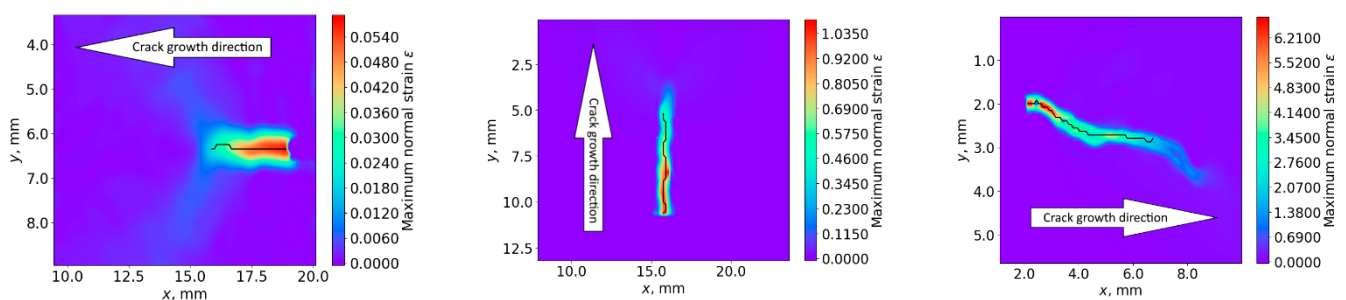
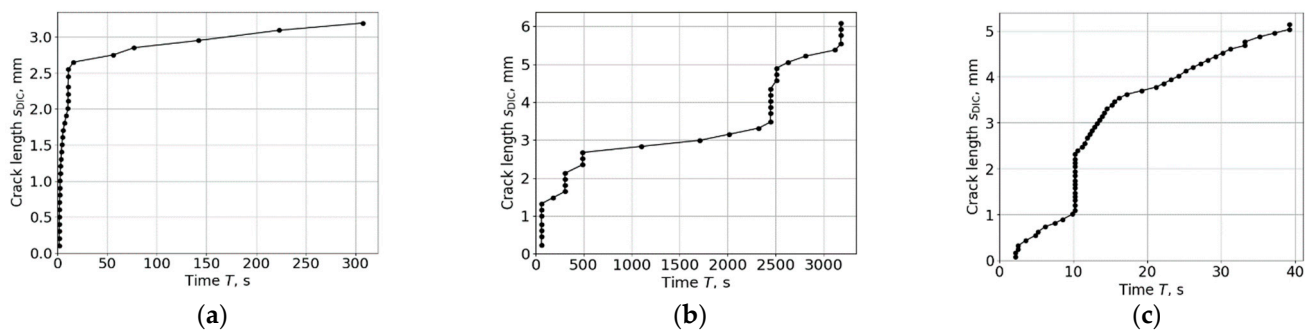


Figure 7. Cont.



**Figure 7.** Field of crack maximum normal strain (**upper row**) and temporal dependencies of the calculated crack length (**lower row**) for rail (a), wheelset (b), and traction clamp (c) samples.

#### 4. Discussion

In this study, we propose a coarse-to-fine approach to fatigue crack detection and measurement in the railway and train parts. It consists of two stages: AE and DIC testing (Figure 8). For such a technique, accurate in-house calibration of both AE and DIC systems is necessary (see Section 2). First of all, analysis of the sample's material and shape must be carried out to set the criteria (1) and (3) for AE and DIC, respectively. To set the criterion (1), one needs to estimate acoustic emissivity of the inspected samples. Proper positioning of AE sensors and minimizing the location error  $dl_{AE}$  require measurements of sound velocity and sensitivity of the AE sensors [48]. To set criterion (3),  $\varepsilon_{TDIC}$  value needs to be defined. Based on  $dl_{AE}$  and available DIC system, we may calculate the optimal parameters  $\beta$  and  $f$  of the optical system. For proper strain measurements across the whole image, the DIC system also needs advanced geometrical calibration [49].

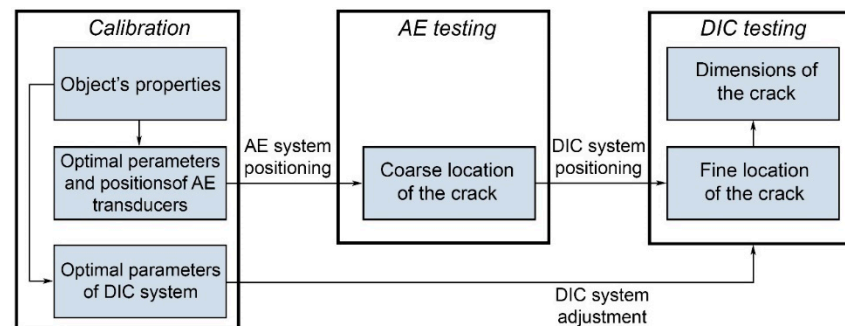


**Figure 8.** Proposed protocol for AE–DIC inspection.

After the calibration stage, AE sensors must be installed on the inspected part for monitoring a fatigue crack's appearance and coarse evaluation of its location. If criterion (1) is fulfilled, the DIC system may be guided to the calculated position of the AE source. Immediate navigation of DIC system to this area allows fine measurement of the crack's location, real-time tracking of its geometrical features, and damage prevention.

The key advantage of the proposed AE–DIC approach is the early detection of defects in railway infrastructure components. This enables studying the defect growth dynamics in real time using the DIC technique. In this case, the investigated sample will be in its natural environment. Thus, it is possible to obtain unique experimental data on the evolution of defects specific to normal operation. This data can significantly improve the theoretical models used in assessing the impact of loads on the studied components, and can be used to develop new criteria for the early detection of defects in these components. The proposed approach allows speeding up the monitoring of fatigue cracks due to the localization of AE source and applying DIC specifically in this area. It is not necessary to stop loading for verifying AE sources, due to non-contact and real-time DIC measurements.

In the railway industry, this approach may be useful for fatigue testing of full-scale railway and train parts as a part of automated loading systems for real-time fatigue crack detection and quantification. It might be efficient and reliable for the samples of various materials and shapes. Though we verified it for railway and train parts, we believe it will have many more applications in multiple fields. For better performance, this technique may be supplemented with mathematical modeling [50] or any other fatigue crack detection methods [51].

## 5. Conclusions

We proposed a two-stage approach to NDT inspection of rails and two train parts under cyclic loading. It is based on sequential application of AE and DIC techniques, and is suitable for real-time evaluation.

We introduced AE criterion as the ratio of the location maximum  $N_{\max}$  in the histogram  $N(l)$  to the mean value  $N_{\text{mean}}$  over all intervals, except for the maximum. This value provides both fatigue crack detection and its coarse location. DIC enables verification of the defect presence and refinement of its position. The DIC criterion for defect detection is reaching the normal strain threshold value  $\varepsilon_{\text{TDIC}}$ .

Experimental results clearly indicate the efficiency of AE for early detection and coarse location of fatigue cracks, and excellent DIC capabilities in terms of its geometrical measurements. In practice, AE might be applied for timely notification of crack appearance and guidance of the DIC system to the area of the crack for quantitative evaluation. The combination of these techniques reveals a promising basis for real-time and non-destructive monitoring rails and train parts.

**Author Contributions:** Conceptualization, A.M. (Alexander Machikhin); methodology, A.M. (Alexander Machikhin) and A.K.; software, V.B. (Vladimir Bardakov); validation, D.Z., A.P. and A.M. (Artem Marchenkov); formal analysis, V.B. (Vera Barat); investigation, A.P.; resources, N.M.; data curation, M.S.; writing—original draft preparation, A.M. (Artem Marchenkov) and A.P.; writing—review and editing, V.B. (Vera Barat); visualization, A.P.; supervision, A.M. (Alexander Machikhin); project administration, D.Z.; funding acquisition, A.M. (Alexander Machikhin). All authors have read and agreed to the published version of the manuscript.

**Funding:** This research was funded by Russian Foundation for Basic Research, Sirius University, JSC Russian Railways and Educational Fund “Talent and success”, grant number 20-38-51019.

**Institutional Review Board Statement:** Not applicable.

**Informed Consent Statement:** Not applicable.

**Data Availability Statement:** The data presented in this study are available on request from the corresponding author.

**Conflicts of Interest:** The authors declare no conflict of interest.

## References

1. Bowler, N.; Gibson, H.R. Fatigue and Its Contribution to Railway Incidents. 2015. Available online: <https://www.sintef.no/globalassets/project/hfc/2015-02-str-fatigue-contribution-to-railway-incident.pdf> (accessed on 1 February 2015).
2. Li, Y.D.; Xu, N.; Wu, X.F.; Guo, W.M.; Shi, J.B. A failure study of the railway rail serviced for heavy cargo trains. *Case Stud. Eng. Fail. Anal.* **2013**, *1*, 243–248. [CrossRef]
3. Smith, R.A. Railway fatigue failures: An overview of a long standing problem. *Mater. Werkst. Entwickl. Fert. Prüfung Eig. Anwend. Tech. Werkst.* **2005**, *36*, 697–705. [CrossRef]
4. Ekberg, A.; Elena, K. Fatigue of railway wheels and rails under rolling contact and thermal loading—An overview. *Wear* **2005**, *258*, 1288–1300. [CrossRef]
5. Vairagi, P.; Surve, T.; Mandavkar, S.; Mhatre, Y.; Hadal, R. Review of Fatigue Crack Growth and Microstructure of Rail. *Int. J. Eng. Res. (IJERT) NTASU* **2021**, *9*, 575–578. [CrossRef]
6. Chudin, V.V.; Knyazev, D.A.; Timakov, M.V. The simulation of crack growth in rolling stock running wheel disk. *IOP Conf. Ser. Mater. Sci. Eng.* **2020**, *747*, 012015. [CrossRef]
7. Ph Papaelias, M.; Davis, C.R.; Claire, L.D. A review on non-destructive evaluation of rails: State-of-the-art and future development. *Proc. Inst. Mech. Eng. F J. Rail Rapid Transit.* **2008**, *222*, 367–384. [CrossRef]

8. Meleshko, N.V.; Makarova, T.I.; Shazinov, S.E. Ultrasonic Testing of Railway Transport Units with Phased Array Flaw Detectors. *NDT World* **2015**, *18*, 72–76.
9. Kuppam Chetty, R.M.; Joshuva, A.; Nikhit Mathew, S.P.; Lokeshwaran, M.; Mohamed Shiham, S.; Rajasekaran, C. A comprehensive review on rail wheel crack inspection system. *J. Mech.* **2020**, *15*, 168–184. [[CrossRef](#)]
10. Grosse, C.; Ohtsu, M. *Acoustic Emission Testing, Basics for Research-Applications in Civil Engineering*; Springer: Berlin/Heidelberg, Germany, 2008; p. 406. [[CrossRef](#)]
11. McCrory, J.P.; Pearson, M.R.; Pullin, R.; Holford, K.M. Optimisation of acoustic emission wavestreaming for structural health monitoring. *Struct. Health Monit.* **2020**, *19*, 2007–2022. [[CrossRef](#)]
12. Harris, D.O.; Dunegan, H.L. Continuous monitoring of fatigue-crack growth by acoustic-emission techniques. *Exp. Mech.* **1974**, *14*, 71–81. [[CrossRef](#)]
13. Barat, V.; Marchenkov, A.; Elizarov, S. Estimation of Fatigue Crack AE Emissivity Based on the Palmer–Heald Model. *Appl. Sci.* **2019**, *9*, 4851. [[CrossRef](#)]
14. Roberts, T.M.; Talebzadeh, M. Acoustic emission monitoring of fatigue crack propagation. *J. Constr. Steel Res.* **2003**, *59*, 695–712. [[CrossRef](#)]
15. Megid, W.A.; Chainey, M.-A.; Lebrun, P.; Hay, D.R. Monitoring fatigue cracks on eyebars of steel bridges using acoustic emission: A case study. *Eng. Fract. Mech.* **2019**, *211*, 198–208. [[CrossRef](#)]
16. Saeedifar, M.; Zarouchas, D. Damage characterization of laminated composites using acoustic emission: A review. *Compos. Part B-Eng.* **2020**, *195*, 108039. [[CrossRef](#)]
17. Bruzelius, K.; Mba, D. An initial investigation on the potential applicability of Acoustic Emission to rail track fault detection. *NDT&E Int* **2004**, *37*, 507–516. [[CrossRef](#)]
18. Bassim, M.N.; St Lawrence, S.; Liu, C.D. Detection of the onset of fatigue crack growth in rail steels using acoustic emission. *Eng. Fract. Mech.* **1994**, *47*, 207–214. [[CrossRef](#)]
19. Hao, Q.; Zhang, X.; Wang, K.; Shen, Y.; Wang, Y. A signal-adapted wavelet design method for acoustic emission signals of rail cracks. *Appl. Acoust.* **2018**, *139*, 251–258. [[CrossRef](#)]
20. Li, D.; Sze, K.; Kuang, C.; Ghee Koh, C. Rail crack monitoring based on Tsallis synchrosqueezed wavelet entropy of acoustic emission signals: A field study. *Struct. Health Monit.* **2018**, *17*, 1410–1424. [[CrossRef](#)]
21. Suwansin, W.; Phasukkit, P. Deep learning-based acoustic emission scheme for nondestructive localization of cracks in train rails under a load. *Sensors* **2021**, *21*, 272. [[CrossRef](#)]
22. Carboni, M.; Andrea, G. Feasibility of an Acoustic emission based structural health monitoring for railway axle under fretting fatigue damage. In Proceedings of the 14th International Conference of the Slovenian Society for Non-Destructive Testing Application of Contemporary Non-Destructive Testing in Engineering, Portorož, Slovenia, 4–6 September 2017; pp. 65–72.
23. Deng, X.-J.; Xui, G.-J.; Liu, S.-Q. Research on Fatigue Crack Detection of Rail Vehicle Axle Based on Acoustic Emission. In Proceedings of the 10th International Workshop on Structural Health Monitoring, Stanford, CA, USA, 1–3 September 2015. [[CrossRef](#)]
24. Bruni, S.; Carboni, M.; Crivelli, D.; Guagliano, M.; Rolek, P. A Preliminary Analysis about the Application of Acoustic Emission and low Frequency Vibration Methods to the Structural Health Monitoring of Railway Axles. *Chem. Eng. Trans.* **2013**, *33*, 697–702. [[CrossRef](#)]
25. Bobrov, A.L.; Stepanova, L.N. Studying the parameters of acoustic emission signals during inspection of cast parts of a freight car truck. *Russ. J. Nondestruct* **2013**, *49*, 722–727. [[CrossRef](#)]
26. Stepanova, L.N.; Kabanov, S.I.; Lebedev, E.Y. Acoustic Emission Diagnostics of Freight Car Bogie Cast Pieces. *Transp. Res. Proc.* **2022**, *61*, 547–555. [[CrossRef](#)]
27. Schreier, H.; Orteu, J.-J.; Sutton, M.A. *Image Correlation for Shape, Motion and Deformation Measurements*; Springer: New York, NY, USA, 2009; p. 322. [[CrossRef](#)]
28. Brynk, T.; Kurzydowski, K.J. Coupling of ultrasounds with the Portevin–Le Chatelier serrations as observed in aluminium-magnesium alloy in mini-samples tensile tests. *Scr. Mater.* **2020**, *174*, 14–18. [[CrossRef](#)]
29. Gu, J.; Pathak, N.; Freed, S.; Todorov, E.; Kim, H. Application of the Nondestructive Evaluation (NDE) Method to Evaluate the Sheared Edge Quality and Edge Cracking. *Form. Future* **2021**, 1585–1593. [[CrossRef](#)]
30. Bakuckas, J.G., Jr.; Stonaker, K.; Stanley, D.; Tian, Y.; Kulak, M.; Chang, P.-Y.; Freisthler, M.; Rodrigues, M.R.B.; Chaves, C.E. Evaluation of adhesively bonded repairs to fuselage structure subjected to environmental conditions. In Proceedings of the 34th ICAF Conference and 28th ICAF Symposium, Helsinki, Finland, 1–5 June 2015; Volume 1, pp. 349–366.
31. Alam, S.Y.; Saliba, J.; Loukili, A. Fracture examination in concrete through combined digital image correlation and acoustic emission techniques. *Constr. Build. Mater.* **2014**, *69*, 232–242. [[CrossRef](#)]
32. Rouchier, S.; Foray, G.; Godin, N.; Woloszyn, M.; Roux, J.-J. Damage monitoring in fibre reinforced mortar by combined digital image correlation and acoustic emission. *Constr. Build. Mater.* **2013**, *38*, 371–380. [[CrossRef](#)]
33. Aggelis, D.G.; Verbruggen, S.; Tsangouri, E.; Tysmans, T.; Hemelrijck, V. Characterization of mechanical performance of concrete beams with external reinforcement by acoustic emission and digital image correlation. *Constr. Build. Mater.* **2013**, *47*, 1037–1045. [[CrossRef](#)]
34. Pullin, R.; Eaton, M.J.; Hensman, J.J.; Holford, K.M.; Worden, K.; Evans, S.L. Validation of Acoustic Emission (AE) Crack Detection in Aerospace Grade Steel Using Digital Image Correlation. *Int. J. Appl. Mech. Mater.* **2010**, *24*, 221–226. [[CrossRef](#)]

35. Pullin, R.; Clarke, A.; Eaton, M.J.; Holford, K.M.; Evans, S.L.; McCorry, J.P. Detection of cracking in gear teeth using Acoustic Emission. *Appl. Mech. Mater.* **2010**, *24*, 45–50. [[CrossRef](#)]
36. Shrama, K.; Al-Jumaili, S.K.; Pullin, R.; Clarke, A.; Evans, S.L. On the Use of Acoustic Emission and Digital Image Correlation for Welded Joints Damage Characterization. *J. Appl. Comput. Mech.* **2019**, *5*, 381–389. [[CrossRef](#)]
37. Swain, D.; Binu, B.; Purushothaman, K.K.; Rao, G.S.; Thomas, B.P.; Kurian, T.; Narayanan, R.; Philip, J. Use of full-field measurements for understanding acoustic emission (AE) signals from 15CDV6 ESR steel specimens. *Procedia Struct. Integr.* **2019**, *14*, 207–214. [[CrossRef](#)]
38. Tanvir, F.; Sattar, T.; Mba, D.; Edwards, G. Identification of fatigue damage evaluation using entropy of acoustic emission waveform. *SN Appl. Sci.* **2020**, *2*, 1–15. [[CrossRef](#)]
39. Zhang, Z.; Yang, G.; Hu, K. Prediction of Fatigue Crack Growth in Gas Turbine Engine Blades Using Acoustic Emission. *Sensors* **2018**, *18*, 1321. [[CrossRef](#)] [[PubMed](#)]
40. Meyer, K.A.; Gren, D.; Ahlström, J.; Ekberg, A. A method for in-field railhead crack detection using digital image correlation. *Int. J. Rail Transp.* **2022**, *10*, 675–694. [[CrossRef](#)]
41. Barat, V.; Marchenkov, A.; Ivanov, V.; Bardakov, V.; Elizarov, S.; Machikhin, A. Empirical Approach to Defect Detection Probability by Acoustic Emission Testing. *Appl. Sci.* **2021**, *11*, 9429. [[CrossRef](#)]
42. Gehri, N.; Mata-Falcón, J.; Kaufmann, W. Automated crack detection and measurement based on digital image correlation. *Constr. Build. Mater.* **2020**, *256*, 119383. [[CrossRef](#)]
43. Panwitt, H.; Köster, P.; Sander, M. Automated crack length measurement for mixed mode fatigue cracks using digital image correlation. *Procedia Struct. Integr.* **2022**, *39*, 20–33. [[CrossRef](#)]
44. Chai, M.; Lai, C.; Xu, W.; Duan, Q.; Zhang, Z.; Song, Y. Characterization of Fatigue Crack Growth Based on Acoustic Emission Multi-Parameter Analysis. *Materials* **2022**, *15*, 6665. [[CrossRef](#)] [[PubMed](#)]
45. Aggelis, D.; Kordatos, E.; Matikas, T. Acoustic emission for fatigue damage characterization in metal plates. *Mech. Res. Commun.* **2011**, *38*, 106–110. [[CrossRef](#)]
46. Barile, C.; Casavola, C.; Pappalettera, G.; Kannan, V.P. Application of different acoustic emission descriptors in damage assessment of fiber reinforced plastics: A comprehensive review. *Eng. Fract. Mech.* **2020**, *235*, 107083. [[CrossRef](#)]
47. Chai, M.; Hou, X.; Zhang, Z.; Duan, Q. Identification and prediction of fatigue crack growth under different stress ratios using acoustic emission data. *Int. J. Fatigue* **2022**, *160*, 106860. [[CrossRef](#)]
48. EN 13554:2011; Non-Destructive Testing—Acoustic Emission Testing—General Principles. Available online: <https://standards.iteh.ai/catalog/standards/cen/1818c70a-d3d8-47f6-a360-e0216f2ff2b1/en-13554-2011> (accessed on 15 March 2011).
49. Sebastian, C.; Patterson, E.A. Calibration of a digital image correlation system. *Exp. Tech.* **2015**, *39*, 21–29. [[CrossRef](#)]
50. Bardakov, V.; Marchenkov, A.; Poroykov, A.; Machikhin, A.; Sharikova, M.; Meleshko, N. Feasibility of Digital Image Correlation for Fatigue Cracks Detection under Dynamic Loading. *Sensors* **2021**, *21*, 6457. [[CrossRef](#)] [[PubMed](#)]
51. Bjørheim, F.; Siriwardane, S.C.; Pavlou, D. A review of fatigue damage detection and measurement techniques. *Int. J. Fatigue* **2022**, *154*, 106556. [[CrossRef](#)]